ECOLOGICAL ENGINEERING & ENVIRONMENTAL TECHNOLOGY

Ecological Engineering & Environmental Technology, 2026, 27(9), 132–148
https://doi.org/10.12912/27197050/225760
ISSN 2719–7050, License CC-BY 4.0

Received: 2026.07.03
Accepted: 2026.07.31
Published: 2026.08.15

A transferable decision-support framework coupling land-cover and land surface temperature simulation for automated green-blue-grey mitigation allocation in data-scarce tropical watersheds

Rohiman La Ode[1], Soma Andang Suryana[2*], Arif Astuti[3], Marwiji Muhammad Yusuf Fadhel[4]

[1] Master of Forestry Science Study Program, Faculty of Forestry, Hasanuddin University, Makassar, South Sulawesi 90245, Indonesia
[2] Watershed Management Laboratory, Faculty of Forestry, Hasanuddin University, Makassar, South Sulawesi 90245, Indonesia
[3] Forestry and Environment Integrated Laboratory, Faculty of Forestry, Hasanuddin University, Makassar, South Sulawesi 90245, Indonesia
[4] Forest Hydrology and Watershed Management Research Group, Faculty of Forestry, Hasanuddin University, Makassar, South Sulawesi 90245, Indonesia
* Corresponding author's e-mail: s_andangs@unhas.ac.id

ABSTRACT

Most land-cover simulations end at a predictive map and leave the engineering question – what mitigation to build, and where – unanswered, an omission that is most acute in data-scarce tropical watersheds lacking dense climatic or hydrometric instrumentation. This study develops and demonstrates a reproducible, four-module decision-support framework, termed coupled thermal–land-cover mitigation allocation (CTMA), that chains land-cover and land surface temperature (LST) forecasting to an automated green–blue–grey mitigation prescription using only openly available Earth-observation data. The framework was demonstrated on the Wanggu watershed, Southeast Sulawesi, Indonesia, using multitemporal Landsat 8 OLI/TIRS imagery (2015, 2020, 2025), a cellular automata–Markov chain (CA-Markov) model coupled to an artificial neural network multi-layer perceptron (ANN-MLP) transition sub-model, and a transition-specific empirical LST-warming model requiring no external climate forcing. Classification reached a kappa accuracy of 86.59%, and the coupled projection was validated by hindcast against the observed 2025 map (Kno = 0.9128, Klocation = 0.9501, K-standard = 0.8940). Rather than inferring causation from correlation, a multiple regression showed that impervious and bare cover independently raised mean LST by 1.24 °C after controlling for the decadal trend ($p = 0.036$; model $R^2 = 0.88$), corroborating the surface-energy-balance mechanism. Under a business-as-usual scenario the LST class above 42 °C is projected to expand by 123% by 2035 and 8,471.18 ha to exceed warming thresholds; the framework then translated this forecast into 28 coded green–blue–grey directives spanning the watershed, dominated by downstream infiltration works (22.19%), mid-watershed water-control terracing (21.40%), and upstream gully-plug structures (14.68%). The contribution is a transferable, low-data workflow that converts environmental simulation into an actionable ecological-engineering prescription.

Keywords: decision-support framework, land surface temperature simulation, CA-Markov, green–blue–grey infrastructure, spatial multi-criteria allocation, data-scarce watersheds.

INTRODUCTION

The conversion of vegetated land into impervious built-up surfaces is one of the most consequential anthropogenic perturbations of the surface energy balance, reducing evapotranspirative cooling and raising land surface temperature (LST) until the urban heat island (UHI) effect emerges (Bokaie et al., 2016; Zhang et al., 2024). In rapidly urbanizing tropical watersheds, this thermal signal is not merely a climatic nuisance; it is an engineering problem whose spatial distribution can, in principle, be forecast and counteracted through targeted ecological intervention. Framing surface warming as an engineerable phenomenon requires two capabilities that have rarely been combined in a single watershed-scale study: a dynamic simulation that projects where land conversion and warming will occur, and a decision rule that translates that projection into what mitigation should be built and where.

The Wanggu watershed is among the priority watersheds in Southeast Sulawesi because it flows through Kendari City, the provincial centre of government, education, and industry, before discharging into Kendari Bay. Accelerated by nickel-driven economic growth and the associated in-migration (Iskandar, 2019; Lèbre et al., 2020), the watershed has experienced sustained conversion of forest and agricultural land into settlements and open land, with consequent declines in hydrological function and increases in sedimentation (Hema et al., 2021; Analuddin et al., 2023). As vegetation is replaced by exposed or sealed surfaces, surface albedo and heat storage rise, and the limited remaining open land cannot dissipate the additional load (Arshad et al., 2022; Jamali et al., 2022). The loss of green space therefore couples directly to thermal degradation, a linkage repeatedly demonstrated across tropical and sub-tropical cities (Dutta et al., 2021; Liou et al., 2024; Tafesse and Suryabhagavan, 2019).

Dynamic spatial modeling has become a standard instrument for anticipating such change. Among available approaches, the cellular automata–Markov chain (CA-Markov) model is widely adopted because it merges the temporal predictive strength of Markov chains with the spatially explicit neighbourhood logic of cellular automata, and because it is readily extended with driver variables (Kushwaha et al., 2021; Xu et al., 2022; Getu and Bhat, 2022). Coupling CA-Markov to an artificial neural network multi-layer perceptron (ANN-MLP) transition sub-model further improves the representation of non-linear relationships between drivers and conversion potential (Xu et al., 2022). The wider shift toward machine-learning and remote-sensing–driven spatial modeling in environmental engineering has proven particularly effective in data-scarce tropical watersheds of Sulawesi, where neural-network and ensemble algorithms have outperformed conventional statistical methods for hazard and susceptibility mapping (Soma et al., 2019; Marwiji et al., 2026; Turahmansyah et al., 2026). However, most watershed applications stop at the land cover map and treat the thermal consequence, if it is considered at all, as a descriptive afterthought rather than as a modeled, mitigable output.

The gap this study addresses is therefore not the availability of any single technique but the absence of a reproducible workflow that closes the loop from forecast to intervention. Three limitations recur in the literature. First, land-cover and thermal projections are produced in isolation and rarely coupled; where land use and surface temperature are examined together, the analysis is typically retrospective and descriptive (Abdullah-Al-Faisal et al., 2022; Njoku and Tenenbaum, 2022; Tafesse and Suryabhagavan, 2019), so the forward thermal consequence of a projected land-cover trajectory is left unquantified. Second, driver analyses lean on bivariate correlation and then speak in the language of causation, an inferential overreach that weakens the evidential basis for any prescription. Third, even where a heat forecast exists, it is seldom converted – through a transparent, transferable rule – into a spatially explicit engineering design; green–blue–grey infrastructure, an integrated ecological-engineering response to combined thermal and hydrological stress (Kumar et al., 2024), is typically allocated by expert judgement rather than by a model-based, auditable decision procedure. These limitations are most consequential in data-scarce settings, where dense climatic and hydrometric networks are unavailable and decisions must rest on open Earth-observation data (Marwiji et al., 2026).

Accordingly, this study develops and demonstrates a reproducible, four-module decision-support framework – coupled thermal–land-cover mitigation allocation (CTMA) – that (i) classifies and validates land cover from multitemporal Landsat imagery; (ii) couples a CA-Markov/ANN-MLP land-cover projection with a transition-specific empirical LST-warming model, validated by hindcast and requiring no external climate forcing; (iii) attributes the thermal response to cover change through association screening and a multivariate regression anchored in the surface-energy-balance mechanism rather than in correlation; and (iv) translates the coupled forecast, via a transparent multi-criteria overlay, into an automated green–blue–grey mitigation prescription. The methodological contribution is the framework itself – a transferable, low-data pipeline from observation to engineered mitigation – demonstrated here on the Wanggu watershed as a representative data-scarce tropical catchment rather than as the object of study in its own right.

MATERIALS AND METHODS

Study area

The Wanggu watershed (±45,760.70 ha) spans 26 sub-watersheds across three administrative units – Kendari City, Konawe Regency, and South Konawe Regency – discharging downstream into Kendari Bay and rising upstream into forested highlands (Figure 1). The climate is semi-arid tropical, with mean annual rainfall of approximately 189.68 mm and a mean annual temperature near 32 °C. The downstream zone has absorbed intense infrastructure development, including road widening, new settlements, commercial estates, and an airstrip (Jurumai et al., 2023). The basin ultimately drains toward Kendari Bay, where upstream land-use and mining activity have elevated sediment and dissolved-metal loads in the receiving waters (Wibowo et al., 2020). The watershed is dominated by Kambisol soils (24,562.79 ha; 53.68%), followed by Podsolik (35.88%) and Organosol (10.40%) (Table 1, Figure 2). These orders differ in thermal-infiltration behaviour: the finer-textured Kambisol and Podsolik retain heat and moisture and support a deep solum suited to agriculture, whereas organic-rich Organosol occupies the low-lying coastal margin. Soil texture conditions the surface energy and water balance and therefore the thermal response examined here. Terrain is predominantly flat to gentle (slope 0–8% over 56.21% of the area).

The CTMA framework

The coupled thermal–land-cover mitigation allocation framework is organised into four sequential modules that move from observation to an engineered prescription (Figure 3). Module 1 (observation and validation) classifies multitemporal Landsat imagery into land-cover maps, validates them against ground reference points, and retrieves LST for the observed epochs. Module 2 (coupled forecasting) projects land cover to a target year with a CA-Markov/ANN-MLP model and propagates a transition-specific empirical warming model to forecast LST, with the coupled projection validated by hindcast against an independent observed epoch. Module 3 (statistical attribution) screens candidate drivers with Cramer's V and quantifies the

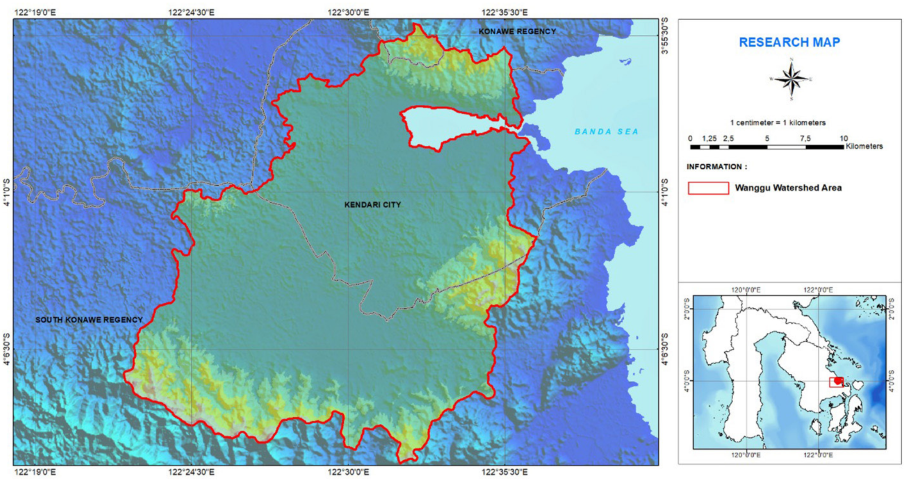

Figure 1. Study area map of the Wanggu watershed, Southeast Sulawesi, Indonesia

Table 1. Soil orders of the Wanggu watershed

No.	Soil order	Area (ha)	%
1	Kambisol	24,562.79	53.68
2	Podsolik	16,418.95	35.88
3	Organosol	4,757.22	10.40
	Total	45,760.70	100

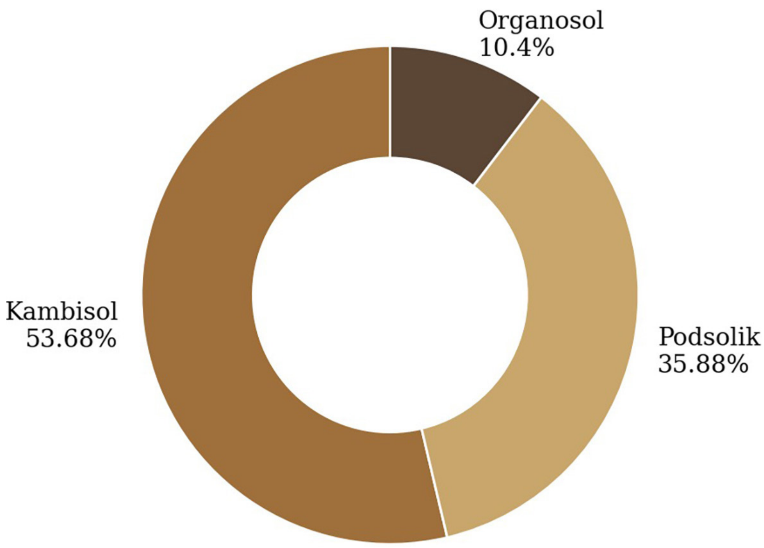

Figure 2. Soil-order composition of the Wanggu watershed

cover–temperature relationship with a multivariate regression interpreted through the surface-energy-balance mechanism. Module 4 (decision allocation) overlays the forecast warming with watershed morphology, land criticality, forest function, and the spatial plan to assign every parcel a coded green–blue–grey mitigation directive. Each module uses only openly available Earth-observation and public-agency data, so the framework is transferable to any data-scarce watershed; the Wanggu watershed serves as the demonstration case. Image processing used QGIS and ArcGIS 10.8; dynamic modeling used the Land Change modeler within Idrisi Selva/TerrSet.

Image preparation and processing

Landsat 8 OLI/TIRS Collection 2 Level-1 scenes for 2015, 2020, and 2025 were obtained from the USGS EarthExplorer portal (https://earthexplorer.usgs.gov). A six-band composite (bands 2–7) was assembled after layer stacking, area-of-interest clipping to the watershed boundary, and radiometric correction. National Digital Elevation Model (DEMNAS, ~8.3 m) and Indonesian Topographic Map (RBI) data were obtained from the Geospatial Information Agency (BIG); population and agricultural statistics were obtained from Statistics Indonesia (BPS).

Land cover classification and validation

Land cover was interpreted by maximum-likelihood supervised classification with polygon training areas, using a band 6-5-4 composite for vegetation discrimination, into thirteen classes following the Ministry of Environment and Forestry scheme (Ministry of Environment and Forestry, 2020). Classification accuracy was assessed against ground reference data through a confusion matrix yielding overall, user, and producer accuracy and the kappa coefficient (Nguyen, 2015). Reference points for 2025 were collected by field ground check; 2015 and 2020 references were drawn from high-resolution Google Earth imagery.

The number of validation points was determined with the Slovin formula (Adrian et al., 2023):

$$n = N / (1 + N e^2) \tag{1}$$

where: n is the sample size, N the population (here the classified area), and e the tolerated error (0.05).

The procedure yielded 211 points allocated across classes by stratified random sampling weighted by class area and accessibility. Kappa accuracy was computed as:

$$K = [N\, \Sigma_i\, x_{ii} - \Sigma_i\, (x_{i+} x_{+i})] / [N^2 - \Sigma_i\, (x_{i+} x_{+i})] \times 100\% \quad (2)$$

where: N is the total number of points, x_{ii} the diagonal (agreement) elements, and x_{i+}, x_{+i} the row and column marginals.

A minimum kappa of 85% was required (Sampurno and Thoriq, 2016).

Land surface temperature retrieval

LST was retrieved from the TIRS thermal band (band 10) following the standard radiative-transfer chain. Digital numbers were first converted to top-of-atmosphere spectral radiance:

$$L\lambda = M\_L\ Q\_cal + A\_L \quad (3)$$

where: M_L and A_L are the band-specific multiplicative and additive rescaling factors and Q_cal the quantized DN. Spectral radiance was converted to at-sensor brightness temperature:

$$BT = K_2 / ln(K_1 / L\lambda + 1) - 273.15 \quad (4)$$

where: K_1 and K_2 the thermal conversion constants.

The normalized difference vegetation index and the proportion of vegetation were computed as:

$$NDVI = (NIR - Red) / (NIR + Red) \quad (5)$$

$$P_v = [(NDVI - NDVI\_min) / (NDVI\_max - NDVI\_min)]^2 \quad (6)$$

Land surface emissivity (ε) was estimated from P_v, and LST in degrees Celsius was obtained as:

$$LST = BT / [1 + (\lambda\ BT / \rho)\ ln\ \varepsilon] \quad (7)$$

where: λ is the emitted radiance wavelength and ρ a thermal constant (1.438×10^{-2} m·K).

Retrieved temperatures were classified into thermal ranges for 2015 and 2025 and overlaid in QGIS to quantify per-class warming.

Driving factors

Five candidate drivers were entered into the model: distance from roads, distance from rivers, population density, elevation, and slope. Euclidean-distance surfaces were generated in ArcGIS; slope and elevation were derived from DEMNAS; population density was classed per SNI 03-1733-2004 (Saraswati, 2010). The strength of association between each candidate

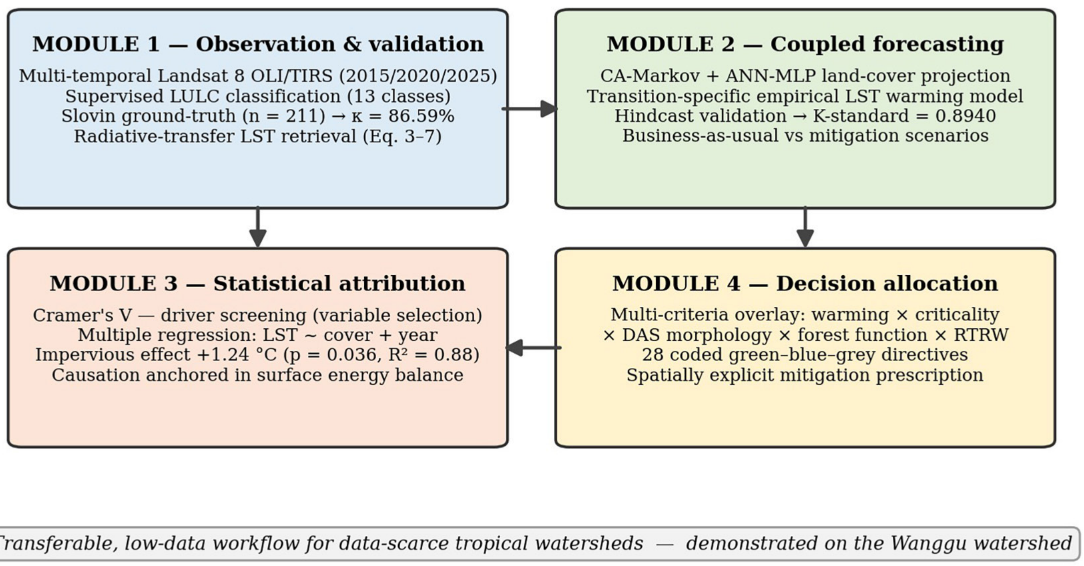

Figure 3. The four-module coupled thermal–land-cover mitigation allocation (CTMA) framework, from Earth-observation input to an automated green–blue–grey mitigation prescription

driver and land-cover change was measured with Cramer's V (range 0–1); this served strictly as an association-based variable-screening step for the transition sub-model, values above 0.10 being retained as informative predictors (Batjoli et al., 2025). Cramer's V was not interpreted as a measure of causal effect.

The cover–temperature relationship was quantified with a multiple linear regression rather than with bivariate correlation, so that the effect of one cover type could be estimated while controlling for others and for the decadal baseline shift. Per-class mean LST for 2015 and 2025 was pooled (n = 26) and regressed on two indicator variables – impervious/bare cover and vegetated cover (cropland and water as reference) – and a year term. Standardized coefficients, the coefficient of determination, and p-values were reported. Causal interpretation was anchored in the surface-energy-balance mechanism, with the regression treated as corroborating, not establishing, that mechanism.

Coupled CA-Markov / ANN-MLP projection

Land cover transitions were modeled in the land change modeler (LCM) using a Markov chain to estimate the transition-probability matrix and an ANN-MLP sub-model to derive transition potentials from the five driver layers; cellular automata then allocated change spatially under neighbourhood contiguity. The ANN-MLP was chosen because, in comparable South Sulawesi watersheds, neural-network optimization of causative factors has outperformed purely statistical models (Soma et al., 2019). To support reproducibility, the MLP was run in the LCM automatic-training mode with the following configuration: one hidden layer; a balanced pixel sample drawn per transition with a 50%/50% training–testing split; start and end learning rates of 0.01 and 0.001, respectively; momentum 0.5; a sigmoid activation function; and a maximum of 10.000 iterations with early stopping on the root-mean-square error. These are the TerrSet/Idrisi LCM defaults and are stated explicitly so the run can be replicated. The full 13 × 13 transition-probability matrix (2015–2025) is provided as a supplementary artifact.

The projection was validated by hindcast: the model was calibrated on 2015–2020, used to predict 2025, and compared cell-by-cell against the independently interpreted 2025 map with the multi-resolution categorical VALIDATE procedure. Agreement was quantified with the full Kappa suite – Kno, Klocation, and K-standard – against a minimum K-standard threshold of 0.70 (Latue and Rakuasa, 2023). Only after passing this hindcast was the model driven by the 2015–2025 transition matrix to project 2035 land cover.

LST for 2035 was forecast with a transition-specific empirical warming model that requires no external climate forcing – an intentional choice for data-scarce watersheds where downscaled climate projections are unavailable. For every observed land-cover transition t, a mean annual warming rate was derived from the 2015–2025 LST change, and applied to the corresponding parcels of the projected 2035 map:

$$LST_{(2035)} = LST_{(2025)} + \\ + \Sigma_t\,(\Delta LST\_t \,/\, \Delta t) \cdot \Delta t\_proj \tag{8}$$

where: ΔLST_t is the decadal temperature change of transition t, Δt = 10 yr the calibration interval, and Δt_proj the projection horizon.

The model rests on an explicit stationarity assumption – that transition-specific warming rates persist over the projection horizon – which was probed by a sensitivity analysis perturbing the rates by ±20%, and framed as two scenarios: a business-as-usual scenario (observed 2015–2025 trajectory continued) and a mitigation scenario (warming rates of parcels receiving green directives reduced toward the vegetated-class baseline). Retrieval uncertainty (±2 °C, native TIRS resolution) was propagated to bound the projected class areas.

Ecological-engineering mitigation design

Areas projected to both warm and lose forest cover by 2035 were isolated as the area of interest for mitigation. This layer was overlaid with watershed morphology, national critical-land status, forest function, and the provincial spatial plan (RTRW) to assign each parcel a coded mitigation directive combining green (vegetative) and blue–grey (civil-technical) features:

$$Directive = f(region\ function, \\ land\ criticality,\ DAS\ morphology) \tag{9}$$

Green features comprised reforestation, enrichment planting, agroforestry, urban greening, community forest, and restoration; blue–grey features comprised terraces, gully plugs, check dams, infiltration wells, biopores, and water-retention structures, consistent with integrated green–blue–grey infrastructure practice (Kumar et al., 2024).

RESULTS AND DISCUSSION

Land cover classification and accuracy

Supervised classification of the 2015, 2020, and 2025 imagery resolved the thirteen-class land cover distribution of the watershed (Table 2). Validation against the 211 ground-check points gave an overall accuracy of 88.15% (186/211) and a kappa accuracy of 86.59%, exceeding the 85% threshold. Per-class user's and producer's accuracy (Table 3) was highest for the dominant, spectrally distinct classes – secondary dryland forest (user's 95.9%, producer's 83.9%), settlement (97.8%, 100%), and paddy field (100%, 87.0%) – and lowest for the spectrally ambiguous shrub and minor dryland-farming classes (user's 50%), reflecting the documented shrub–degraded-forest confusion in Indonesian imagery. The full 13 × 13 confusion matrix is provided as a supplementary artifact. Overall agreement was

Table 2. Land cover area in the Wanggu watershed, 2015–2025

Land cover class	2015 (ha)	2020 (ha)	2025 (ha)
Airport (Bdr)	130.44	130.44	130.44
Secondary dryland forest (Hs)	13,871.32	12,890.87	13,590.76
Secondary mangrove forest (Hms)	46.66	38.94	37.50
Open land (Lt)	1,174.13	2,044.40	2,061.77
Port (Plb)	5.07	5.07	5.07
Settlement (Pmk)	9,370.43	10,572.08	9,862.55
Plantation (Pkb)	245.08	241.33	241.33
Dryland farming (Pt)	1,314.86	1,199.18	857.14
Mixed dryland farming (Pc)	12,821.05	11,781.25	12,564.25
Paddy field (Sw)	4,262.25	4,202.86	4,244.50
Pasture/shrub (Sb)	2,149.36	2,267.42	1,813.96
Fishpond (Tm)	327.53	344.34	308.85
Water body (Air)	49.71	49.67	49.76
Total	45,760.70	45,760.70	45,760.70

Table 3. Per-class accuracy of the 2025 land cover classification (confusion matrix, n = 211)

Class	Classified ∑	Reference ∑	Correct	User's acc. (%)	Producer's acc. (%)
Airport (Bdr)	1	1	1	100.0	100.0
Secondary dryland forest (Hs)	49	56	47	95.9	83.9
Secondary mangrove forest (Hms)	1	1	1	100.0	100.0
Open land (Lt)	10	12	9	90.0	75.0
Port (Plb)	1	1	1	100.0	100.0
Settlement (Pmk)	46	45	45	97.8	100.0
Plantation (Pkb)	1	1	1	100.0	100.0
Dryland farming (Pt)	8	5	4	50.0	80.0
Mixed dryland farming (Pc)	57	53	47	82.5	88.7
Paddy field (Sw)	20	23	20	100.0	87.0
Pasture/shrub (Sb)	14	10	7	50.0	70.0
Fishpond (Tm)	2	2	2	100.0	100.0
Water body (Air)	1	1	1	100.0	100.0
Total / Overall	211	211	186	88.15	κ = 86.59

Table 4. Cramer's V association between drivers and land cover change (overall and selected classes)

Class / aggregate	Population density	Distance from road	Distance from river	Elevation	Slope
Settlement (Pmk)	0.3515	0.5355	0.0314	0.2928	0.3104
Secondary dryland forest (Hs)	0.2739	0.6948	0.1507	0.7112	0.5596
Paddy field (Sw)	0.2184	0.1935	0.0621	0.1815	0.2288
Mixed dryland farming (Pc)	0.1579	0.0873	0.0458	0.0671	0.0975
Open land (Lt)	0.1521	0.1121	0.0121	0.1058	0.0635
Overall V	0.1628	0.2394	0.0605	0.2074	0.1751

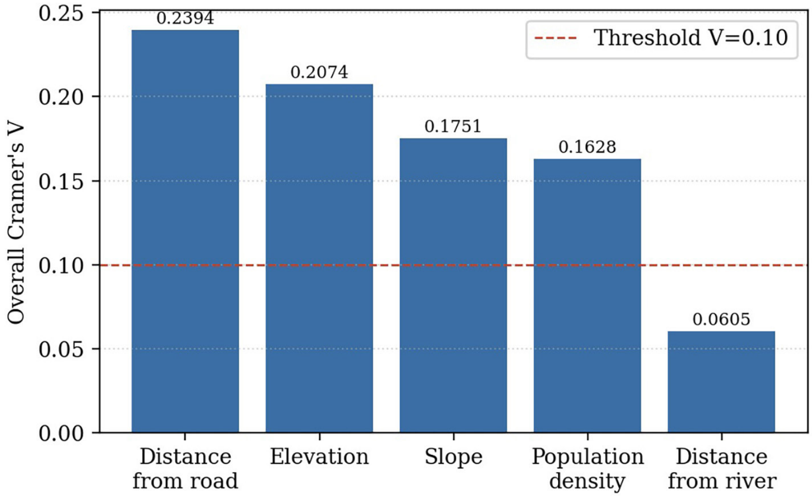

Figure 4. Overall Cramer's V of the five land cover change drivers; the dashed line marks the V = 0.10 significance threshold

186/211 (88.15%), giving a kappa accuracy of 86.59% (Equation 2).

Land cover change, 2015–2025

Between 2015 and 2025 the watershed lost vegetated cover to non-vegetated classes. Open land expanded from 1,174.13 to 2,061.77 ha (+887.64 ha) and settlements increased by 492.12 ha, while secondary dryland forest contracted, its dominant conversion being to mixed dryland agriculture (809.35 ha), with additional losses to open land (226.83 ha), shrub (59.33 ha), and paddy (20.68 ha). These transitions reflect the combined pressure of land demand and anthropogenic activity reported for comparable settings (Demissie et al., 2017; Setiawan et al., 2024).

Driving factors of land cover change

Cramer's V screened the association between each candidate predictor and land cover change (Table 4, Figure 4). Across all classes, distance from road showed the strongest overall association with conversion (V = 0.2394), followed by elevation (0.2074) and slope (0.1751); distance from river was weakest (0.0605). These values guided variable selection for the transition sub-model and indicate where conversion is most likely, not why the surface warms. The control was sharpest for secondary dryland forest, whose conversion was governed by elevation (V = 0.7112), road proximity (0.6948), and slope (0.5596); settlement change was driven by road proximity (0.5355) and population density (0.3515). The road result is mechanistically coherent: proximity to roads lowers the cost of access and therefore the threshold for clearing, so forest near roads is the most exposed to conversion. The elevation control imposes a hard limit – no conversion was recorded above 375 m a.s.l. – consistent with topographic gating of land development elsewhere (Njoku and Tenenbaum, 2022; Li et al., 2020).

Surface temperature dynamics, 2015–2025

Retrieved LST confirmed pronounced decadal warming (Table 5, Figure 5). In 2015 surface temperature ranged from 19 to 30 °C and was dominated by the 28–32 °C class (28,840.02 ha; 60.60%). By 2025 the range had shifted upward to 22–46 °C, the 34–42 °C class dominated (38,265.55 ha; 80.41%), and a new class above 42 °C appeared over 554.12 ha. The cooler lower tail had effectively disappeared, the warming concentrated in settlements and built-up land – exactly the classes that expanded – while remaining vegetation in the upstream zone retained the lowest temperatures.

Attribution of the thermal response to land cover

The thermal signal mapped onto cover type (Table 6, Figure 6). Mean LST was highest under built and bare surfaces – settlement rose from 31.51 to 38.51 °C and open land from 29.97 to 37.14 °C – and lowest under secondary dryland forest (26.99 to 33.54 °C), which remained the coolest class in both years. Bivariate correlation between the decadal change in each class's area and LST was consistent with this pattern (Figure 7) – open land (r = 0.758) and settlement (r = 0.214) positive, vegetated and water classes negative (shrub r = −0.840; secondary mangrove r = −0.836; plantation r = −0.747) – but such correlations describe association only and cannot, on their own, support a causal claim.

To place the attribution on firmer ground, mean LST (pooled 2015 and 2025, n = 26) was regressed on cover type and year (Table 7). The model explained 88% of the variance ($R^2 = 0.88$; F-test $p < 0.001$), and, crucially, impervious/bare cover independently raised mean LST by 1.24 °C after controlling for the strong decadal baseline shift and for vegetation (standardized $\beta = 0.19$, $p = 0.036$); vegetated cover carried the expected cooling sign ($\beta = -0.12$) though it did not reach significance at this aggregate

Table 5. Land surface temperature distribution, 2015 and 2025

2015 class (°C)	Area (ha)	%	2025 class (°C)	Area (ha)	%
<20	741.87	1.56	<24	1,148.10	2.41
20–24	2,495.86	5.24	24–29	351.97	0.74
24–28	7,013.97	14.74	29–34	7,268.20	15.27
28–32	28,840.02	60.60	34–42	38,265.55	80.41
>32	8,496.23	17.85	>42	554.12	1.16
Total	45,760.70	100	Total	45,760.70	100

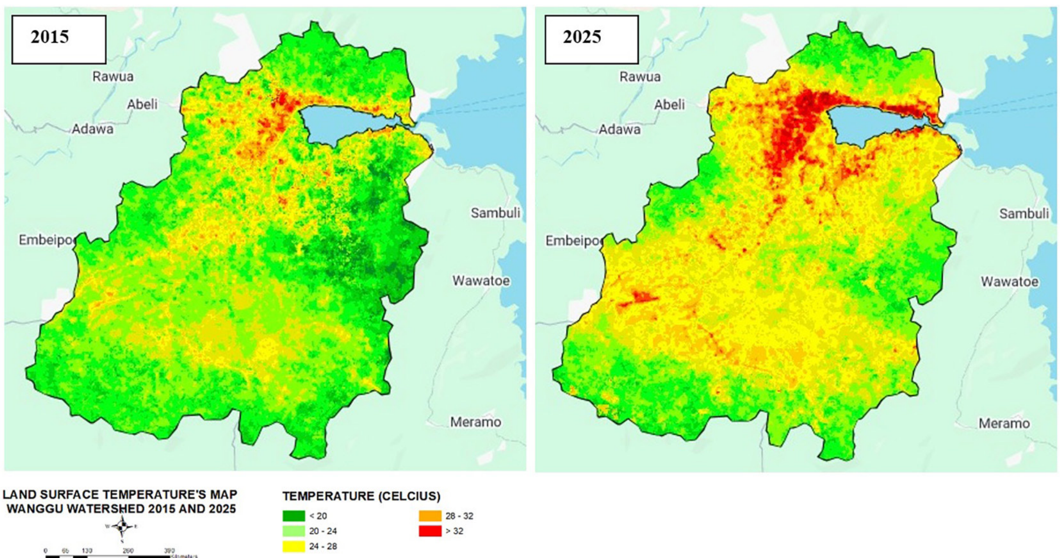

Figure 5. Spatial distribution of land surface temperature across the Wanggu watershed in 2015 and 2025, showing the upward thermal shift concentrated in settlement and built-up zones

Table 6. Mean LST per land cover class and its Pearson correlation with surface temperature

Land cover class	Mean LST 2015 (°C)	Mean LST 2025 (°C)	Pearson r (area Δ vs LST)
Airport	32.85	38.25	n/a
Secondary dryland forest	26.99	33.54	−0.078
Secondary mangrove forest	30.81	35.35	−0.836
Open land	29.97	37.14	0.758
Port	31.15	36.03	n/a
Settlement	31.51	38.51	0.214
Plantation	31.32	35.42	−0.747
Dryland farming	30.08	35.14	−0.997*
Mixed dryland farming	30.00	35.28	−0.036
Paddy field	31.36	35.01	−0.091
Shrub/pasture	30.04	35.70	−0.840
Fishpond	31.17	35.46	−0.687
Water body	30.99	36.32	−0.711

Note: * Significant at $p < 0.05$.

Table 7. Multiple regression of mean land surface temperature on cover type and year (pooled per-class means, n = 26)

Predictor	Coefficient (°C)	Standardized β	p-value
Intercept	30.54	—	<0.001
Impervious / bare cover	+1.24	0.19	0.036
Vegetated cover	−0.75	−0.12	0.168
Year (2015→2025)	+5.30	0.90	<0.001
Model	$R^2 = 0.88$	adj. $R^2 = 0.87$	F $p < 0.001$

sample size. A companion model of the decadal warming rate likewise found impervious classes warming 1.53 °C more than the reference over the decade ($p = 0.049$), with the mean warming ordered built/bare (6.11 °C) > vegetation (5.23 °C) > cropland/water (4.58 °C). Because the sign, magnitude, and ordering of these coefficients follow directly from the surface-energy-balance mechanism – impervious surfaces suppress evapotranspiration and store more sensible heat – the regression is interpreted as corroborating that physical mechanism rather than as establishing causation from correlation. This reading is consistent with South Sulawesi susceptibility studies in which the shift from dense to sparse vegetation is the dominant degradation factor (Soma and Kubota, 2018). The cover-type effect is, moreover, the surface expression of the well-documented inverse relationship between vegetation greenness (NDVI) and land surface temperature reported across tropical and subtropical settings (Dutta et al., 2021; Njoku and Tenenbaum, 2022; Tafesse and Suryabhagavan, 2019); notably, NDVI is already embedded in the present retrieval through the vegetation-proportion and emissivity terms (Equations 5–6), so the thermal contrast between vegetated and impervious classes follows directly from the radiative physics rather than from a post-hoc correlation. The analysis remains observational and rests on aggregate per-class means; the causal claim is therefore mechanistic, and the driver screening (Cramer's V) identifies only where conversion is most likely, not *why* the surface warms.

Projection of land cover and temperature to 2035

The hindcast validation supported forward projection. Calibrated on 2015–2020 and tested cell-by-cell against the independently interpreted 2025 map with the multi-resolution VALIDATE procedure, the CA-Markov/ANN-MLP model returned Kno = 0.9128, Klocation = 0.9501, and K-standard = 0.8940 (89.40% agreement over 14

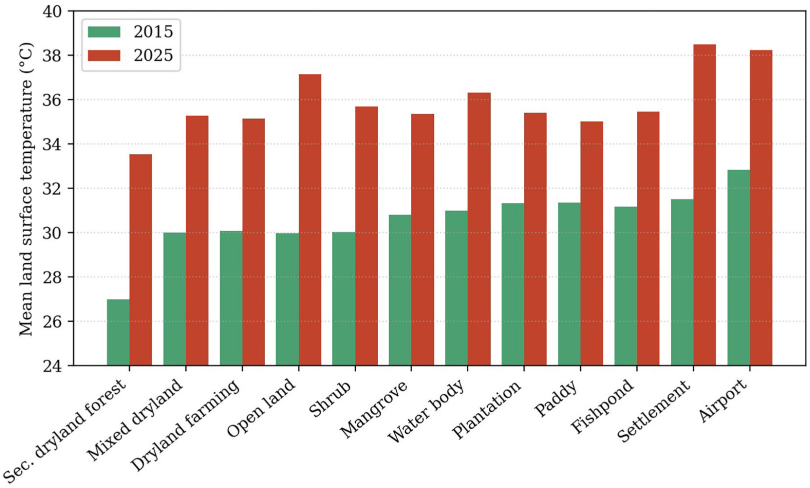

Figure 6. Mean land surface temperature per land cover class, 2015 versus 2025. Built and bare classes are warmest; secondary dryland forest is coolest in both years

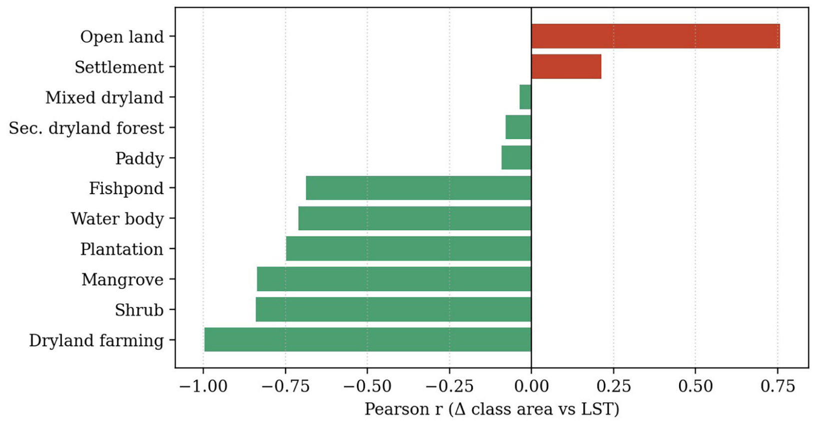

Figure 7. Pearson correlation between the decadal change in each land cover class's area and land surface temperature. Positive (warming) associations in red, negative (cooling) in green

categories), well above the 0.70 threshold; the high Klocation confirms that the model placed change correctly, not merely in the right quantity. Only after passing this test was the model driven by the 2015–2025 transition matrix to project 2035, which forecast continued forest loss: secondary dryland forest declines by a further 1,096.55 ha – the largest single loss – while open land and settlements expand by 602.62 and 451.40 ha, concentrated in the Kendari City–South Konawe boundary zone (Figure 10).

Propagating these transitions through the transition-specific warming model (Equation 8) projected a continued upward thermal shift (Table 8, Figure 8), mapped spatially in Figure 9. Under the business-as-usual scenario, the class above 42 °C grows from 554.12 to 1,236.92 ha (+123.22%) and the 29–34 °C class comes to dominate (27,853.61 ha). The highest per-transition warming coefficients – open-land-to-built (1.145) and cropland-to-open (1.107) – localize the most acute future heat risk, whereas the lowest (water-to-cropland, 0.349) marks stable terrain. The ±20% sensitivity test shifted the projected >42 °C area between roughly 1,050 and 1,420 ha without changing the direction or ranking of the thermal shift, and the ±2 °C retrieval bound translates into class-area uncertainty of the same order; the projection is therefore robust in trajectory though conditional in exact magnitude. Under the mitigation scenario – the 8,288.50 ha (18.1% of the watershed) assigned vegetative green directives held at the vegetated-class warming rate rather than the conversion trajectory – an illustrative calculation, assuming these parcels avoid 35–45% of their share of the projected threshold exceedance, keeps an estimated 240–310 ha below the 42 °C threshold and lowers the projected >42 °C class

Table 8. Projected LST distribution under the business-as-usual scenario, 2025 versus 2035

Class (°C)	2025 (ha)	2035 (ha)	Change (ha)	Change (%)
<24	1,148.10	252.64	−895.46	−77.99
24–29	351.97	2,525.98	+2,174.01	+617.67
29–34	7,268.20	27,853.61	+20,585.41	+283.23
34–42	38,265.55	13,891.06	−24,374.49	−63.70
>42	554.12	1,236.92	+682.81	+123.22
Total	45,760.70	45,760.70	—	—

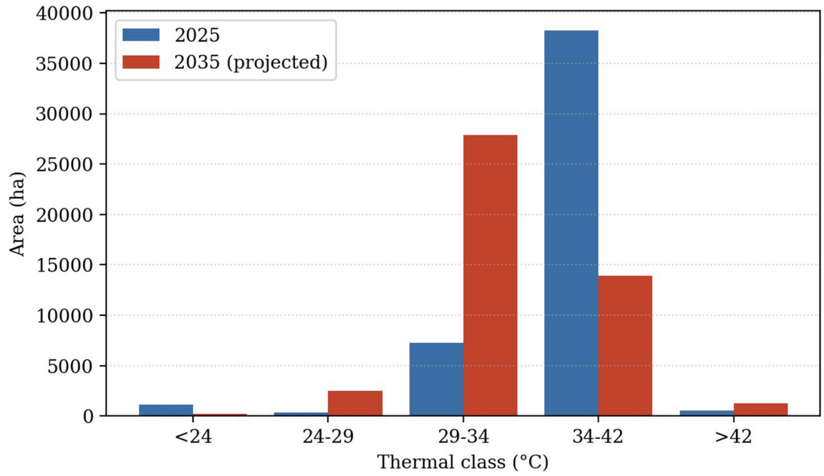

Figure 8. Projected redistribution of land surface temperature classes between 2025 and 2035; the >42 °C class expands by 123%

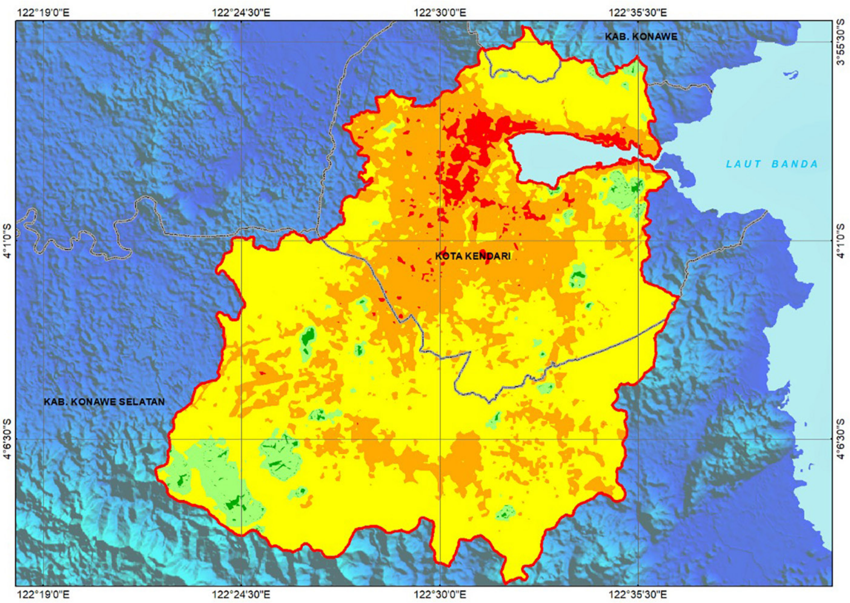

Figure 9. Projected spatial distribution of land surface temperature across the Wanggu watershed in 2035, with the highest classes concentrated in the expanding built-up and open-land zones

from 1,236.92 ha to roughly 930–1.000 ha. This estimate is indicative rather than a calibrated forecast, but it quantifies the direction and order of magnitude of the thermal benefit the framework is designed to deliver, and it establishes the counterfactual against which the mitigation portfolio can later be evaluated.

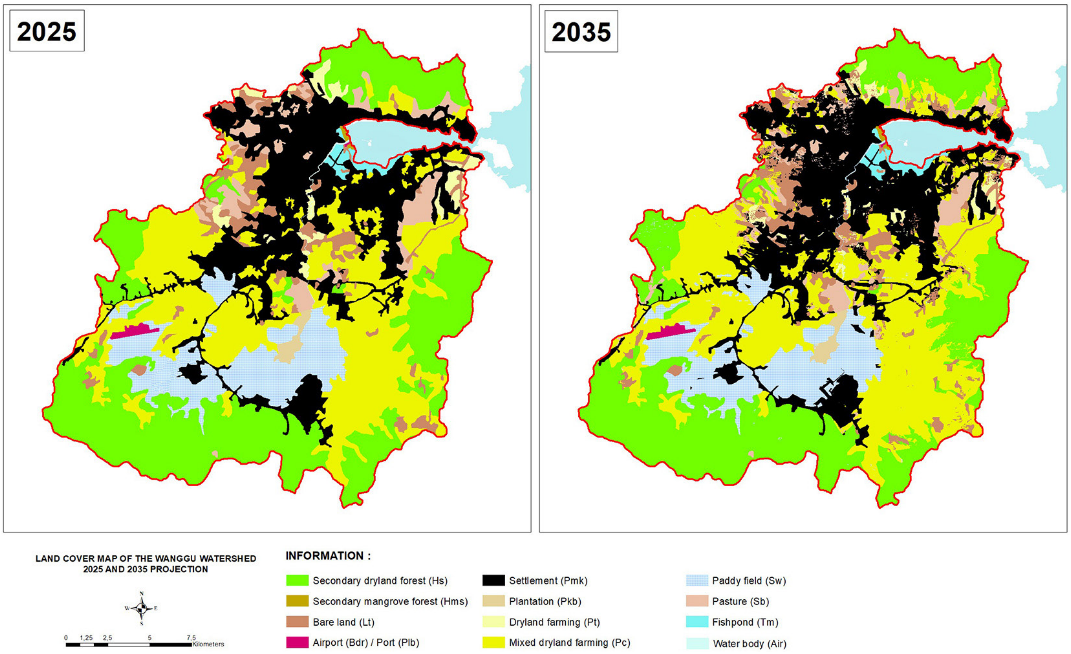

Figure 10. Land cover map for 2025 and the CA-Markov/ANN-MLP projection for 2035, showing forest contraction and the expansion of open land and settlements in the Kendari City–South Konawe boundary zone

Ecological-engineering mitigation portfolio

Overlaying the projected 2035 land cover with watershed morphology, critical-land status, forest function, and the provincial spatial plan (RTRW) yielded 28 coded mitigation directives spanning the entire watershed (45,760.70 ha), each pairing green (vegetative) with blue–grey (civil-technical) features (Table 9, Figures 11 and 12). Within this framework, 8,471.18 ha were flagged as the priority zone projected to exceed the warming thresholds by 2035 and thus targeted for immediate intervention. The portfolio is spatially differentiated: the largest allocations are infiltration-well and biopore directives in the downstream cultivated lowland (PBST3, 10,155.30 ha; 22.19%), water-control terraces in the mid-watershed (PBST2, 9,791.27 ha; 21.40%), and gully-plug/terrace works in the protected upstream forest (RLST1, 6,718.77 ha; 14.68%). This allocation operationalizes the causal findings: green features are concentrated where vegetation most strongly suppresses LST, and blue–grey features where impervious conversion and slope most strongly amplify it, consistent with integrated green–blue–grey infrastructure design (Kumar et al., 2024).

Model uncertainty

Three sources of uncertainty temper the interpretation. First, thermal retrieval from Landsat TIRS carries an inherent accuracy of approximately ±2 °C at native resolution, so

Table 9. Principal ecological-engineering mitigation directives (selected from 28 combinations)

Code	Green feature (vegetative)	Blue–grey feature (civil-technical)	Area (ha)	%
PBST3	—	Infiltration well / biopore / retention	10,155.30	22.19
PBST2	—	Water-control terrace	9,791.27	21.40
RLST1	—	Gully plug / terrace	6,718.77	14.68
PBST1	—	Water-control terrace	4,616.67	10.09
PBVEG1ST1	Permanent-stand greening / non-timber	Water-control terrace	3,262.08	7.13
PBVEG2	Greening / community forest	—	1,734.69	3.79

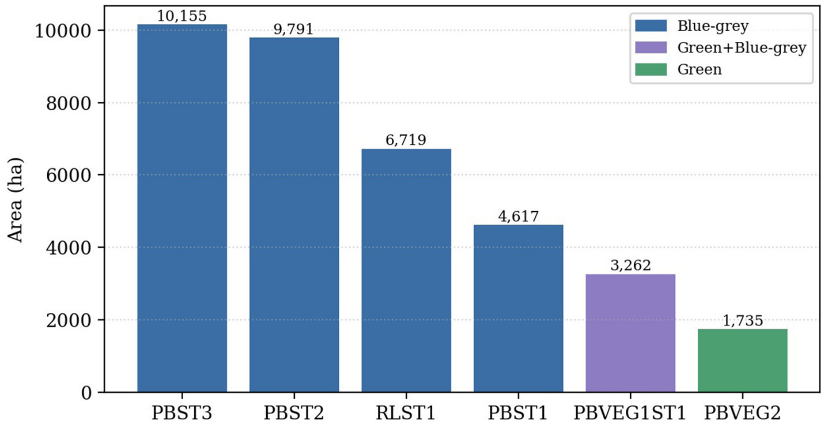

Figure 11. Area of the principal ecological-engineering mitigation directives, classified by green, blue–grey, and combined feature type

individual class means should be read as central estimates rather than exact values. Second, the projection assumes that the 2015–2025 transition probabilities and warming rates remain stationary to 2035; abrupt policy, economic, or climatic shifts would alter the trajectory, and the projected figures are therefore conditional rather than deterministic. Because the transition-specific warming rates are derived from the same 2015–2025 interval they project, the thermal forecast is validated indirectly – through the independent hindcast of its land-cover driver (K-standard = 0.8940) and the ±20% sensitivity test – rather than against a withheld thermal epoch. An aggregate test based on the annual watershed-mean LST is deliberately not used for this purpose, because the watershed mean is dominated by stable forest and agricultural cover and is confounded by inter-annual atmospheric and cloud-cover variability; it therefore does not isolate the conversion-driven thermal signal, which operates at the class rather than the catchment-average level. This is precisely why the framework attributes warming through the per-class, within-year multivariate model (Table 7) – which is invariant to inter-annual

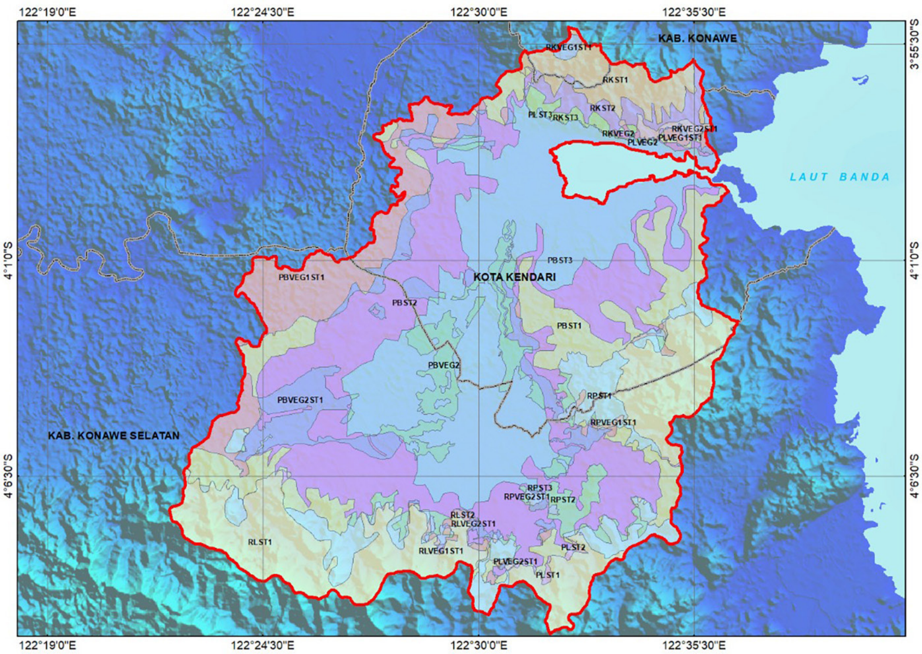

Figure 12. Spatial distribution of the green–blue–grey ecological-engineering mitigation directives across the Wanggu watershed, derived from the overlay of the projected 2035 warming zones with watershed morphology, critical-land status, forest function, and provincial spatial-planning zones

atmospheric fluctuation – and validates the projection through its independently hindcast land-cover driver, rather than through an aggregate LST trend. A fully class-resolved thermal validation would require an additional per-class LST layer for an intermediate epoch, and the framework is structured so that such a layer can be inserted without altering the workflow. Third, classification residuals – most visibly the documented confusion between shrub and degraded forest in Indonesian imagery – propagate into both the change matrix and the thermal attribution. The strength of the validation statistics (kappa 86.59%; K-standard 0.8940) constrains these uncertainties to within accepted limits, but the mitigation portfolio is best treated as a risk-prioritized design to be refined with field verification rather than as a fixed prescription.

CONCLUSIONS

A reproducible four-module framework – Coupled Thermal–Land-cover Mitigation Allocation – was developed to convert open Earth-observation data into an automated green–blue–grey mitigation prescription and demonstrated on the Wanggu watershed. Its observation module classified land cover at a kappa accuracy of 86.59%; its forecasting module passed hindcast validation with Kno = 0.9128, Klocation = 0.9501, and K-standard = 0.8940. Between 2015 and 2025 the watershed lost vegetated cover, secondary dryland forest declining principally through conversion to mixed dryland agriculture over 809.35 ha while open land expanded by 887.64 ha and settlements by 492.12 ha, with distance from road the strongest statistical association with conversion (Cramer's V = 0.2394) and no conversion above 375 m a.s.l. The attribution module showed that impervious and bare cover independently raised mean land surface temperature by 1.24 °C after controlling for the decadal trend ($p = 0.036$; model $R^2 = 0.88$), a result whose sign and magnitude follow the surface-energy-balance mechanism. Surface temperature rose over the decade, the dominant thermal class shifting from 28–32 °C to 34–42 °C and a class above 42 °C emerging over 554.12 ha, with secondary dryland forest the coolest cover throughout. Under the business-as-usual scenario, secondary dryland forest is projected to decline by a further 1,096.55 ha by 2035, open land and settlements to expand by 602.62 and 451.40 ha, and the class above 42 °C to grow by 123.22%. The allocation module translated this forecast into 28 coded green–blue–grey directives spanning the watershed, dominated by downstream infiltration and biopore works (22.19%), mid-watershed water-control terracing (21.40%), and upstream gully-plug structures (14.68%), with 8,471.18 ha identified as the priority zone projected to exceed the warming thresholds by 2035.

Data and code availability

All input data are open. The Landsat 8 OLI/TIRS Collection 2 Level-1 scenes are available from the USGS EarthExplorer portal (https://earthexplorer.usgs.gov); DEMNAS elevation and RBI topographic data from the Indonesian Geospatial Information Agency (https://tanahair.indonesia.go.id/demnas); and population and agricultural statistics from Statistics Indonesia (BPS). To make the CTMA framework fully reproducible, the following research artifacts are provided as Supplementary Online Material accompanying this submission: SOM S1 – the Google Earth Engine script implementing the NDVI, emissivity, and LST retrieval chain (Equations 3–7); SOM S2 – the land-cover transition-probability matrix (2015–2025); SOM S3 – the ANN-MLP configuration and the multi-resolution VALIDATE report (Kno, Klocation, K-standard); SOM S4 – the full 13 × 13 confusion matrix with per-class user's and producer's accuracy; SOM S5 – the 28-row mitigation decision matrix with its overlay codification rules; and the reproducible regression script for Table 7. The derived land-cover classifications, LST rasters, and mitigation-directive layers are additionally available from the corresponding author on reasonable request. Software: QGIS, ArcGIS 10.8, TerrSet/Idrisi Selva (Land Change Modeler), and Google Earth Engine.

Acknowledgments

The authors thank the USGS and NASA for the Landsat 8 OLI/TIRS datasets and the Indonesian Geospatial Information Agency (BIG) for DEMNAS and RBI data. The authors also thank the anonymous reviewers for constructive feedback. This research received no specific grant from any funding agency in the public, commercial, or not-for-profit sectors. The authors declare no conflict of interest.

REFERENCES

1. Abdullah-Al-Faisal, Rahman, M. S., Kafy, A.-A., Roy, S., Khan, A. R., Rahman, M. M. (2022). Impact on land surface temperature and urban heat island, due to land use/land cover change in Dhaka metropolitan area, using remote sensing and GIS techniques. In *Re-envisioning Advances in Remote Sensing* (pp. 69–102). CRC Press. https://doi.org/10.1201/9781003224624-6
2. Adrian, A., Widiatmaka, W., Munibah, K., Firmansyah, I. (2023). Pola spasial perubahan tutupan lahan/penggunaan lahan menggunakan Google Earth Engine di Kabupaten Majalengka [Spatial patterns of land cover/land use change using Google Earth Engine in Majalengka Regency]. *Jurnal Pembangunan Wilayah dan Kota, 19*(4), 447–463. https://doi.org/10.14710/pwk.v19i4.46254
3. Analuddin, K., Armid, A., Ruslin, R., Sharma, S., Kadidae, L. O., Haya, L. O. M. Y., Septiana, A., Rahim, S., McKenzie, R. A., La Fua, J. (2023). The carrying capacity of estuarine mangroves in maintaining the coastal urban environmental health of Southeast Sulawesi, Indonesia. *Egyptian Journal of Aquatic Research, 49*(3), 327–338. https://doi.org/10.1016/j.ejar.2023.03.002
4. Arshad, S., Ahmad, S. R., Abbas, S., Asharf, A., Siddiqui, N. A., Islam, Z. ul. (2022). Quantifying the contribution of diminishing green spaces and urban sprawl to urban heat island effect in a rapidly urbanizing metropolitan city of Pakistan. *Land Use Policy, 113*, 105874. https://doi.org/10.1016/j.landusepol.2021.105874
5. Batjoli, M. F., Lihawa, F., Lahay, R. J. (2025). Prediksi spasial deforestasi kawasan hutan Taman Nasional Bogani Nani Wartabone menggunakan cellular automata–artificial neural network [Spatial prediction of forest deforestation in Bogani Nani Wartabone National Park using cellular automata–artificial neural network]. *Jurnal Ilmu Lingkungan, 23*(2), 443–451. https://doi.org/10.14710/jil.23.2.443-451
6. Bokaie, M., Zarkesh, M. K., Arasteh, P. D., Hosseini, A. (2016). Assessment of urban heat island based on the relationship between land surface temperature and land use/land cover in Tehran. *Sustainable Cities and Society, 23*, 94–104. https://doi.org/10.1016/j.scs.2016.03.009
7. Demissie, F., Yeshitila, K., Kindu, M., Schneider, T. (2017). Land use/land cover changes and their causes in Libokemkem District of South Gonder, Ethiopia. *Remote Sensing Applications: Society and Environment, 8*, 224–230. https://doi.org/10.1016/j.rsase.2017.10.001
8. Dutta, D., Rahman, A., Paul, S. K., Kundu, A. (2021). Impervious surface growth and its inter-relationship with vegetation cover and land surface temperature in peri-urban areas of Delhi. *Urban Climate, 37*, 100799. https://doi.org/10.1016/j.uclim.2021.100799
9. Getu, K., Bhat, H. G. (2022). Dynamic simulation of urban growth and land use change using an integrated cellular automata and Markov chain models: A case of Bahir Dar city, Ethiopia. *Arabian Journal of Geosciences, 15*(11), 1049. https://doi.org/10.1007/s12517-022-10359-0
10. Hema, H., Assiddieq, M., Ndibale, W., Ilham, I., Wibowo, D. (2021). Analisis kualitas air dengan parameter TSS, BOD, deterjen dan fosfat (PO4) pada Sungai Wanggu Kota Kendari [Water quality analysis using TSS, BOD, detergent, and phosphate (PO4) parameters in the Wanggu River, Kendari City]. *Jurnal Envirotek, 13*(2), 34–40. https://doi.org/10.33005/envirotek.v13i2.126
11. Iskandar, A. (2019). Empowerment of foreign manpower and Indonesian manpower through developing foreign companies in Indonesia. *International Journal of Sciences: Basic and Applied Research, 48*(6), 128–149.
12. Jamali, A. A., Ghorbani Kalkhajeh, R., Randhir, T. O., He, S. (2022). Modeling relationship between land surface temperature anomaly and environmental factors using GEE and Giovanni. *Journal of Environmental Management, 302*, 113970. https://doi.org/10.1016/j.jenvman.2021.113970
13. Jurumai, L. P., Abidin, A. A., Soetrisno, E. T., Wibowo, D. (2023). Impact of population growth and housing development on the riverine environment: Identifying environmental threat and solution in the Wanggu River, Indonesia. *Ecological Modelling, 486*, 110540. https://doi.org/10.1016/j.ecolmodel.2023.110540
14. Kumar, P., Corada, K., Debele, S. E., Emygdio, A. P. M., Abhijith, K. V., Hassan, H., Broomandi, P., Baldauf, R., Calvillo, N., Cao, S.-J., Desrivières, S., Feng, Z., Gallagher, J., Kjeldsen, T. R., Khan, A. A., Khare, M., Kota, S. H., Li, B., Malham, S. K., … Jones, L. (2024). Air pollution abatement from green–blue–grey infrastructure. *The Innovation Geoscience, 2*(4), 100100. https://doi.org/10.59717/j.xinn-geo.2024.100100
15. Kushwaha, K., Singh, M. M., Singh, S. K., Patel, A. (2021). Urban growth modeling using earth observation datasets, cellular automata–Markov chain model and urban metrics to measure urban footprints. *Remote Sensing Applications: Society and Environment, 22*, 100479. https://doi.org/10.1016/j.rsase.2021.100479
16. Latue, P. C., Rakuasa, H. (2023). Analysis of land cover change due to urban growth in Central Ternate District, Ternate City using cellular automata–Markov chain. *Journal of Applied Geospatial Information, 7*(1), 722–728. https://doi.org/10.30871/jagi.v7i1.4653
17. Lèbre, É., Stringer, M., Svobodova, K., Owen, J. R., Kemp, D., Côte, C., Arratia-Solar, A., Valenta, R. K.

(2020). The social and environmental complexities of extracting energy transition metals. *Nature Communications, 11*(1), 4823. https://doi.org/10.1038/s41467-020-18661-9

18. Li, K., Feng, M., Biswas, A., Su, H., Niu, Y., Cao, J. (2020). Driving factors and future prediction of land use and cover change based on satellite remote sensing data by the LCM model: A case study from Gansu Province, China. *Sensors, 20*(10), 2757. https://doi.org/10.3390/s20102757
19. Liou, Y.-A., Tran, D.-P., Nguyen, K.-A. (2024). Spatiotemporal patterns and driving forces of surface urban heat island in Taiwan. *Urban Climate, 53*, 101806. https://doi.org/10.1016/j.uclim.2024.101806
20. Marwiji, M. Y. F., Soma, A. S., Arif, S., Rahmat, S. (2026). Integration of Sentinel-1 synthetic aperture radar and random forest algorithm for high-precision flood hazard modeling in a data-scarce tropical watershed. *Ecological Engineering & Environmental Technology, 27*(2), 198–215. https://doi.org/10.12912/27197050/217188
21. Ministry of Environment and Forestry. (2020). *The state of the world's forests 2020*. FAO and UNEP. https://doi.org/10.4060/ca8642en
22. Nguyen, T. (2015). Optimal ground control points for geometric correction using genetic algorithm with global accuracy. *European Journal of Remote Sensing, 48*(1), 101–120. https://doi.org/10.5721/EuJRS20154807
23. Njoku, E. A., Tenenbaum, D. E. (2022). Quantitative assessment of the relationship between land use/land cover (LULC), topographic elevation and land surface temperature (LST) in Ilorin, Nigeria. *Remote Sensing Applications: Society and Environment, 27*, 100780. https://doi.org/10.1016/j.rsase.2022.100780
24. Sampurno, R., Thoriq, A. (2016). Land cover classification using Landsat 8 Operational Land Imager (OLI) imagery in Sumedang Regency. *Jurnal Teknotan, 10*(2), 61–70. https://doi.org/10.24198/jt.vol10n2.9
25. Saraswati, E. (2010). *Procedures for planning urban residential environments (SNI 03-1733-2004).* National Standardization Agency of Indonesia.
26. Setiawan, O., Rahayu, A. A. D., Samawandana, G., Tata, H. L., Dharmawan, I. W. S., Rachmat, H. H., Suharti, S., Windyoningrum, A., Khotimah, H. (2024). Unraveling land use land cover change, their driving factors, and implication on carbon storage through an integrated modeling approach. *Egyptian Journal of Remote Sensing and Space Science, 27*(4), 615–627. https://doi.org/10.1016/j.ejrs.2024.08.002
27. Soma, A. S., Kubota, T. (2018). Landslide susceptibility map using certainty factor for hazard mitigation in mountainous areas of Ujung-loe watershed in South Sulawesi. *Forest and Society, 2*(1), 79–91. https://doi.org/10.24259/fs.v2i1.3594
28. Soma, A. S., Kubota, T., Mizuno, H. (2019). Optimization of causative factors using logistic regression and artificial neural network models for landslide susceptibility assessment in Ujung Loe Watershed, South Sulawesi Indonesia. *Journal of Mountain Science, 16*(2), 383–401. https://doi.org/10.1007/s11629-018-4884-7
29. Tafesse, B., Suryabhagavan, K. V. (2019). Systematic modeling of impacts of land-use and land-cover changes on land surface temperature in Adama Zuria District, Ethiopia. *Modeling Earth Systems and Environment, 5*(3), 805–817. https://doi.org/10.1007/s40808-018-0567-1
30. Turahmansyah, A. I., Ahmad, A., Soma, A. S., Santi, M. A. (2026). Landslide susceptibility modelling using the weight of evidence and logistic regression approaches in the Balease watershed, Indonesia. *Ecological Engineering & Environmental Technology, 27*(2), 374–389. https://doi.org/10.12912/27197050/217597
31. Wibowo, D., Basri, B., Adami, A., Sumarlin, S., Rosdiana, R., Ndibale, W., Ilham, I. (2020). Analysis of nickel (Ni) in seawater and its distribution in Kendari Bay waters, Southeast Sulawesi. *Indonesian Journal of Chemical Research, 8*(2), 144–150. https://doi.org/10.30598/ijcr.2020.8-wib
32. Xu, T., Zhou, D., Li, Y. (2022). Integrating ANNs and cellular automata–Markov chain to simulate urban expansion with annual land use data. *Land, 11*(7), 1074. https://doi.org/10.3390/land11071074
33. Zhang, M., Yiğit, İ., Adigüzel, F., Hu, C., Chen, E., Siyavuş, A. E., Elmastaş, N., Ustuner, M., Kaya, A. Y. (2024). Impact of urban surfaces on microclimatic conditions and thermal comfort in Burdur, Türkiye. *Atmosphere, 15*(11), 1375. https://doi.org/10.3390/atmos15111375